

# A Metal-Resilient, Remote, Wideband UHF RFID Tag Employing RIS for Prefabricated Construction Component Traceability

Weijie Ge, *Student Member, IEEE*, Lingzhi Luo, *Member, IEEE*, Yaqing Yu, *Member, IEEE*, Xiangyu Zhou, *Member, IEEE*, Jingjing Liu, *Member, IEEE* and Jiang Wu, *Senior Member, IEEE*

**Abstract**—This paper proposes a reactive impedance surface (RIS)-loaded, inductively fed full-wave dipole (FWD) UHF RFID tag designed for metal-mounted and concrete-embedded prefabricated component traceability. The tag employs a small copper loop for inductive feeding, effectively matching both the high impedance of the FWD and the large capacitive component of the RFID integrated circuit across the UHF band. Metal tolerance is achieved by employing the RIS, which can compensate the parasitic capacitance and reduce strong interaction between the antenna and the metal plane. Experimental results demonstrate that the proposed single tag achieves a measured bandwidth ( $|S_{11}| \leq -10$  dB) of 700 MHz (76.5%) and a maximal read distance of 22.62 m. When mounted on metal with the RIS, the bandwidth reduces to 632 MHz (69%), and the maximum reading distance decreases to 20.19 m. Additionally, when embedded in concrete, the antenna loading RIS and metal plane maintains a maximum read distance of 4.63 m, demonstrating robust performance in construction material environments.

**Index Terms**—UHF RFID Tag, Full wave dipole (FWD), Reactive impedance surface (RIS), Remote, Broadband.

## I. INTRODUCTION

The 5G-enabled IoT (5G-IoT) scenarios demand new performance criteria, such as massive connectivity, ultra-low latency, trustworthiness, high reliability, and security for a large number of IoT devices [1]. Radio frequency identification (RFID) technology, known for its low cost, battery-free operation, high information accuracy,

contactless operation, and automatic data updates, is crucial for 5G-IoT ecosystems. However, RFID systems face increasing complex electromagnetic environment across industries. For instance, RFID tags may be mounted on diverse material, including plastic, metal, asphalt or biological surfaces. Thus, tag antennas must be designed to address material-induced obstructions and interferences in varying scenarios.

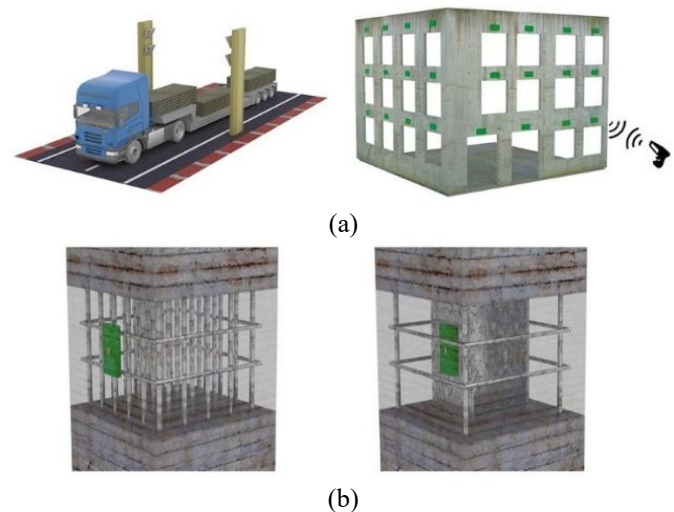


Fig. 1. (a) Illustration of the RFID system used for tracing and tracking prefabricated components. (b) Types of prefabricated components that RFID tags are mounted on or embedded in.

As illustrated in Fig. 1(a), RFID tags are mounted on or embedded within prefabricated components (PCs), while readers are strategically positioned at entry/exit points for tracking. These tags also facilitate automated assembly during construction and quality inspection post-construction. Fig. 1(b) depicts common PCs, including prefabricated concrete components (PCCs) and prefabricated steel components (PSCs). A substantial amount of concrete, acting as a consumable medium, can significantly shorten the reading distance of RFID, while extensive metal networks can cause tags failure due to antenna impedance mismatch [2]. Given these challenges, antennas for PC tracing must meet four key criteria: (1) metal tolerance; (2) high gain to counteract attenuation from lossy media; (3) broad bandwidth to adapt to changes in embedded medium properties; (4) compact size to avoid damage during transportation and installation.

The RFID tag antenna is critical for overcoming interference in complex electromagnetic environments. Most existing

This work was supported by the National Natural Science Foundation of China (62174181), the Fundamental Research Funds for the Central Universities (ZYGX2019Z018), the Innovation Group Project of Sichuan Province (20CXTD0090) and the Postdoctoral Innovative Talent Support Program (BX20240453) (Corresponding author: Jingjing Liu, Yaqing Yu.)

Weijie Ge and Jingjing Liu are with the School of Electronics and Communication Engineering, Sun Yat-sen University and also with Guangdong Provincial Key Laboratory of Sea-Air-Space Communication, Shenzhen 518107, China (e-mail: gewj@mail2.sysu.edu.cn; liujj77@mail.sysu.edu.cn).

Lingzhi Luo is with the Electrical Division of the Department of Engineering at the University of Cambridge, Cambridge CB3 0FA, UK. (e-mail: ll672@cam.ac.uk).

Yaqing Yu is with the NUS (Chongqing) Research Institute, Intelligent Sensing and Artificial Intelligence Center, Chongqing 401123, China. (e-mail: yaqing.yu@nusricq.cn).

Xiangyu Zhou and Jiang Wu are with the Institute of Fundamental and Frontier Sciences, University of Electronic Science and Technology of China, 610054 Chengdu, China. (e-mail: 15937176902@163.com; jiangwu@uestc.edu.cn).

> IoT-53036-2025 <

designs adopt half-wave dipole (HWD) antennas, leveraging advantages such as small electrical size and easy impedance matching [3-5]. However, achieving high gain with HWDs often requires antenna arrays and power dividers, which substantially increases both antenna size and implementation cost. Full-wave dipole (FWD) antennas, by contrast, benefit from larger electrical sizes and exhibit higher gain and broader bandwidth than HWDs. Unfortunately, the presence of extremely high impedance points within the FWD frequency band complicates in-band matching [6]. Some researchers have addressed this issue by optimizing impedance matching, enhancing gain/bandwidth, and reducing profile using parallel HWDs [5]. Thus, resolving the high-impedance matching challenge of FWDs while leveraging their high-gain and wide-bandwidth advantages would be highly beneficial for RFID tag antennas in PC traceability.

In PC traceability scenarios, the widespread metal networks (a major cause of RFID tag failure) highlight the urgent need for metal-resistant antennas. A notable exception is the use of a metal ground to achieve unidirectional gain, which mitigates backside metal interference. Metamaterial-based approaches—including electromagnetic bandgap (EBG) structures [3, 7, 8], artificial magnetic conductor (AMC) structures [9, 10], and high impedance surface (HIS) configurations [11, 12]—have been widely explored for metal-insensitive RFID tags. These structures typically consist of periodic dielectric substrates and various metal patterns. By suppressing surface waves and manipulating reflection phases, they are widely applied in miniaturized antenna design and gain enhancement. For example, an EBG structure with a periodic 2D circular pattern integrated into the ground plane of an RFID microstrip patch antenna effectively suppressed surface waves and slightly extended the reading range [7]. Reference [8] proposed a mushroom-like EBG structure for metal-mounted RFID tags: by tuning the reflection phase to  $90^\circ \pm 45^\circ$ , measurements showed a maximum reading distance of 9 m. More recently, a double-layer symmetric electromagnetic band gap (DLS-EBG) structure has been designed for metallic objects [3]: when mounted on a 300 mm×300 mm metal plate, the antenna achieved a measured bandwidth of 116 MHz and a reading distance of 12.3 m. Additionally, references [9], [10] reported a compact AMC ground plane composed of a narrow rectangular patch-pair array with offset vias; while these designs significantly enhanced radiation performance, their bandwidths remained limited to tens of megahertz. A miniaturized dual-layer RFID tag antenna is proposed in [12], featuring a bandwidth covering the ranges of 830–885 MHz and 910–950 MHz, a gain of –12 dBi, and a reading distance of 1.8 m (with a metal plate) / 2 m (without a metal plate) by introducing a HIS. However, EBG structures achieve electromagnetic wave control at the expense of bandwidth and increased design complexity. Meanwhile, AMCs and HISs necessitate the antenna to be positioned a quarter-wavelength away from the ground, resulting in larger profiles and increased structural volumes. Alternatively, employing high-dielectric-constant

media to reduce profile introduces design complexities and escalates costs.

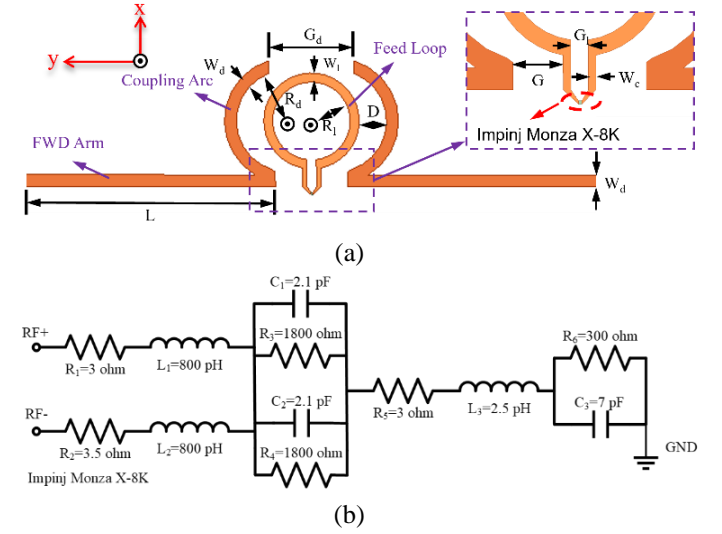


Fig. 2. (a) Geometry of the proposed inductively fed FWD ( $L=85.5$  mm,  $W_d=2$  mm,  $G_d=8.3$  mm,  $W_l=1.5$  mm,  $R_d=8.5$  mm,  $R_l=5$  mm,  $D=1.0$  mm,  $G_l=1.6$  mm,  $G=1.5$  mm,  $W_c=0.7$  mm). (b) The lumped parameter equivalent circuit of Impinj Monza X-8K.

Moreover, many studies have focused on reconfigurable intelligent surfaces for complex electromagnetic environments [13-16], as they regulate electromagnetic waves to mitigate interference, improve communication link quality, and enable efficient energy transmission. Unlike conventional reconfigurable intelligent surfaces that rely on far-field control, reactive impedance surface (RIS) can suppress parasitic capacitance effects from backside metal through near-field regulation—achieving anti-metal functionality without significant bandwidth loss, while maintaining a low profile and simple design. Integrating a RIS layer into the dielectric between the patch and ground plane can effectively expand the bandwidth while reducing the antenna size. This is attributed to the fact that RIS exhibits intermediate properties between an ideal conductor and an ideal magnetic conductor, featuring tunable impedance across these two extremes. Such characteristics enable the adjustment of impedance matching to enhance bandwidth and gain, all while minimizing the overall size [17], [18]. Reference [19] proposed a RIS (a 4×4 array of periodic metallic square patches) to improve antenna bandwidth and gain: at 5.5 GHz, this design achieved a 44.5% bandwidth improvement and a stable gain of 7.2 dBi. The core goal of such RIS-based designs is to minimize adverse antenna-substrate interactions (e.g., mutual coupling between the antenna and its image) while emphasizing beneficial interactions (e.g., favorable spectral trends of stored electrical/magnetic energy), which supports bandwidth enhancement and/or antenna miniaturization.

Furthermore, properly positioning RIS between the radiating patch and ground plane can achieve a  $0^\circ$  reflection phase, facilitating wideband design and improving impedance

> IoT-53036-2025 <

matching [17-20]. Although several RIS-loaded metal-tolerant RFID tag antennas have been proposed, achieving long reading ranges alongside miniaturization and bandwidth enhancement remains a challenge. Given the FWD's wide bandwidth and high gain, coupled with the RIS's simple structure (which avoids excessive bandwidth sacrifice for anti-metal performance), the integration of these two technologies holds significant promise. To meet the traceability requirements of PC, this work represents the first attempt to propose the combination of FWD and RIS for RFID tag antennas.

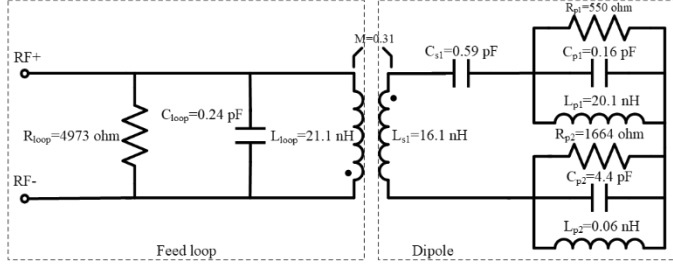


Fig. 3. The lumped parameter equivalent circuit of the proposed inductively fed FWD. (The lumped component values are obtained through ADS fitting)

This paper proposes an inductively fed FWD RFID tag loaded with a RIS for metal-mounted and concrete-embedded applications in PC tracing and tracking. Geometric optimization of the feed loop achieves UHF band impedance matching between the high-impedance FWD and the large capacitive RFID IC. The RIS effectively mitigates metal-induced performance degradation by compensating parasitic capacitance and minimizing antenna-metal plane interactions. Large peak gain and bandwidth were achieved without metal interference. When subjected to metal backside interference, the loadable and detachable RIS structure effectively alleviates performance degradation through parasitic capacitance compensation and reduction of antenna-metal plane interaction. To elucidate the operational mechanism, a hybrid equivalent circuit model incorporating both lumped elements and transmission line theory, based on the physical structure of the antenna, was developed, supplemented by current density and electric field distribution simulations. This design enables long-range reading in complex electromagnetic environments, even accounting for signal loss due to concrete and back metal presence, making it ideal for prefabricated component identification in construction.

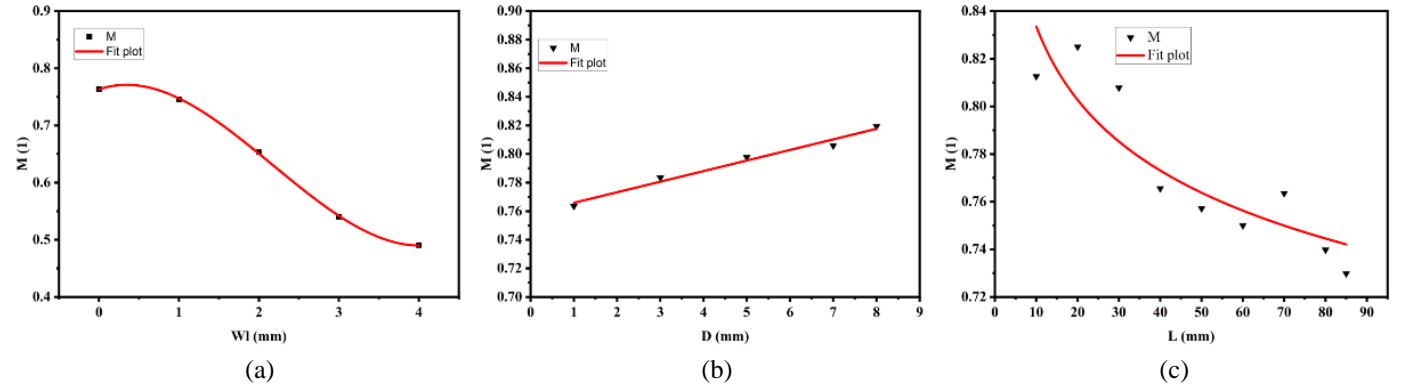


Fig. 4. The coupling strength  $M$  between the feed loop and the coupling arcs varies with three key parameters, as shown in the corresponding subfigures alongside their fitted curves: (a) the metal width of the feed loop ( $W_l$ ); (b) the spacing between the feed loop and the coupling arcs ( $D$ ); and (c) the length of the dipole arms ( $L$ ).

## II. THE PROPOSED TAG DESIGN AND ANALYSIS

### A. The Inductively Fed Broadband Full-Wave Dipole

Fig. 2(a) illustrates the geometry of the proposed tag, featuring a circular inductive feed loop electromagnetically coupled to two FWD arms. To enhance coupling efficiency, the FWD arms incorporate two arc-shaped terminations proximal to the feed loop, named coupling arc. Fabricated on a 1 mm-thick FR4 substrate ( $\epsilon_r = 4.4$ ), the design integrates the Impinj Monza X-8K RFID IC for operation. RFID integrated circuits (ICs) exhibit significant capacitive impedance due to their rectifying diodes, thus requiring conjugate impedance matching with inductive antenna components to achieve optimal power transfer. Small feed loop with inductive matching coupling is widely adopted for inductive feeds in RFID tag designs due to their inherent impedance characteristics. Fig. 2(b) depicts the RFID IC's wideband small-signal model per the manufacturer's

datasheet, revealing a chip impedance of  $14.669 - j157.016 \Omega$  at 915 MHz with a receiving sensitivity of -17 dBm. The proposed antenna connected to the RFID IC is represented by a lumped parameter equivalent circuit for broadband impedance analysis. Fig. 3 presents the antenna's equivalent circuits, where the feed loop is modeled as a parallel RLC resonance circuit ( $R_{loop}, L_{loop}, C_{loop}$ ) [21], [22], while the dipole is represented by two parallel RLC networks ( $R_{pi}, L_{pi}, C_{pi}$ , where  $i = 1, 2$ ) and a series LC circuit ( $L_{s1}, C_{s1}$ ) in cascade, accurately characterizing impedance behavior up to the second parallel resonance [23]. The coupling mechanism between the feed loop and dipole is quantified by the mutual inductance  $M$  between  $L_{loop}$  and  $L_{s1}$ . Based on this equivalent circuit, the input impedance of the proposed tag ( $Z_{ant}$ ) is expressed as [24]:

$$Z_{ant} = Z_{loop} + \frac{(\omega M)^2}{Z_d} \quad (1)$$

here,  $Z_{loop}$  and  $Z_d$  denote the self-impedance of the feed loop



> IoT-53036-2025 <

and dipole, respectively. These impedances are mathematically defined as:

$$Z_{loop} = \frac{1}{\frac{1}{R_{loop}} + j\omega C_{loop} + \frac{1}{j\omega L_{loop}}} \quad (2)$$

$$Z_d = \frac{1}{\frac{1}{R_{p1}} + j\omega C_{p1} + \frac{1}{j\omega L_{p1}}} + \frac{1}{\frac{1}{R_{p2}} + j\omega C_{p2} + \frac{1}{j\omega L_{p2}}} + j\omega L_{s1} + \frac{1}{j\omega C_{s1}} \quad (3)$$

The feed loop functions as an impedance self-matching network, where the equivalent inductance  $L_{loop}$  constitutes the critical design parameter, which can be generated from the following formulas: [25]:

$$L_{loop} = K_1 \mu_0 \frac{n^2 d_{avg}}{1 + K_2 \rho} \quad (4)$$

$$d_{avg} = \frac{(R_l + W_l) + R_l}{2} \quad (5)$$

$$\rho = \frac{W_l}{(R_l + W_l) + R_l} \quad (6)$$

where  $K_1$  and  $K_2$  are 3.836 and 1.72, respectively [26];  $\mu_0$  is the vacuum permeability, which is  $4\pi \times 10^{-7} N/A^2$ ;  $n$  is the number of coil turns ( $n = 1$  in this design);  $d_{avg}$  is the average of inner and outer radius of the feed loop;  $\rho$  is the metal filling rate. Based on the above formulas, initial values of the equivalent circuit components can be derived. It is noteworthy that most of the discrepancies stem from unaccounted pin inductance in the feed loop between the loop and the chip pins (Fig. 2(a)) and geometric approximation errors between octagonal and circular structures (where circular configurations generally yield higher inductance values), the component values calculated by the formula require further fine-tuned and optimized in the ADS. The final optimized component values are presented in Fig. 3. The component values of the circuit are derived from initial calculations of the feed loop and coupling arc inductances, which serve as baseline initial values. Subsequently, all component values are finalized via 3D electromagnetic simulation and fitting to the equivalent circuit impedance in ADS (Advanced Design System). Fitting errors primarily stem from inaccuracies in equivalent model establishment and inherent simulation errors. Notably, the impedance curve discrepancies two methods (initial calculation vs. simulation-fitting) can be extremely small. This is because the component values of the equivalent circuit can be continuously optimized to approximate the impedance parameters of the electromagnetic structure, enabling the error to approach zero asymptotically.

Further investigation of the relationship between the structure of the FWD antenna and the coupling coefficient involves extracting the correlation between the coupling strength coefficient  $M$  and the key physical parameters, guiding subsequent impedance matching adjustments. Fig. 4 illustrates the  $M$  between the feed loop and the coupling arcs, governed primarily by the feed loop's metal width  $W_l$  and spacing  $D$ . Given the coupling mechanism's complexity,  $M$  demonstrates an empirical correlation with geometric parameters, which  $M =$

$-0.04759W_l - 0.07485W_l^2 + 0.01147W_l^3 + 0.0074D + 0.94453L^{-0.0543} + 0.0061983$ . Furthermore, the dipole arm's equivalent circuit parameters follow the geometric scaling laws established in [23]. Through simulation-based polynomial fitting, these functional relationships are incorporated into the circuit's governing equations to resolve element values. This framework enables deterministic tuning of the dipole arms' dual resonance frequencies by optimizing  $L/W_d$ , thereby establishing a theoretical foundation for parameter optimization.

Validation of the equivalent circuit involves comparing the simulated results from ADS with the corresponding antenna results from HFSS, as shown in Fig. 5. One can observe that the results in ADS agree well with the one in HFSS. Due to the small value of  $\omega M$ ,  $Z_{loop}$  offers the primary inductive component, implying that the impedance matching between the IC and the whole antenna is mainly determined by the feed loop. Although  $Z_d$  has a minimal impact on impedance matching, tuning the dipole into resonance is preferable for effective radiation. In our loop-fed design, the FWD was engineered to resonant at its first parallel resonance, i.e., the full-wave resonant state. As aforementioned, the FWD typically suffers from impedance mismatching due to its high input impedance. Nevertheless, owing to the inductive coupling between the feed loop and the dipole, the high input impedance of FWD can be intrinsically transformed into a very small one, as described in (1). Fig. 5 reveals dipole resonance at 915 MHz, evidenced by a resistance curve peak and reactance curve fluctuation, coinciding with optimal IC-antenna matching. The simulated bandwidth reaches 500 MHz (0.7-1.2 GHz), fully encompassing the UHF RFID operational band (860-960 MHz). This broadband performance confirms the feed loop's dual role in achieving both impedance matching and resonance conditioning within the operational band, while preserving the FWD's inherent gain and bandwidth advantages.

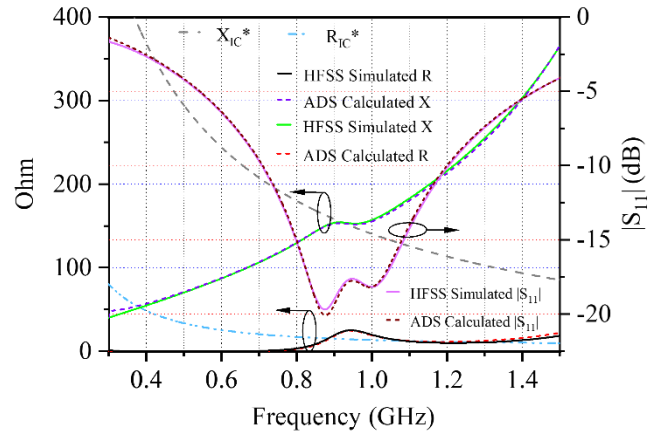


Fig. 5. The comparison of the simulated resistance (R), reactance (X) and  $|S_{11}|$  with HFSS and ADS.  $X_{IC}^*$  and  $R_{IC}^*$  are the conjugate reactance and resistance of the RFID IC.

Additionally, a parametric study was performed to validate the above analysis and to gain insights into antenna optimization, as shown in Fig. 6(a)-(c). When width of the loop  $W_l$  is increased, both the resistance and the inductance decrease,

> IoT-53036-2025 <

as depicted in Fig. 6(a). The inductance, in particular, decreases more prominently due to the reduction of the magnetic flux through the loop, which can be employed to tune the impedance of the proposed antenna for matching with different RFID ICs [27]. Dipole arm elongation  $L$  induces a redshift (move towards low-frequencies) in the resistance peak and reactance fluctuation, as shown in Fig. 6(b), corresponding to extended full-wave resonant wavelengths. Concurrently, resonance amplitude attenuation occurs due to the increased radiative

losses. Coupling distance  $D$  inversely governs loop-dipole interaction strength: larger  $D$  values suppress resonance amplitude and induce slight blueshift (move towards high-frequencies), as shown in Fig. 6(c), enabling precision resonance conditioning through coordinated  $L$ - $D$  optimization. By optimizing the parameters along the path, maximum impedance bandwidth for the proposed antenna can be achieved, thereby determining the optimal structural parameters.

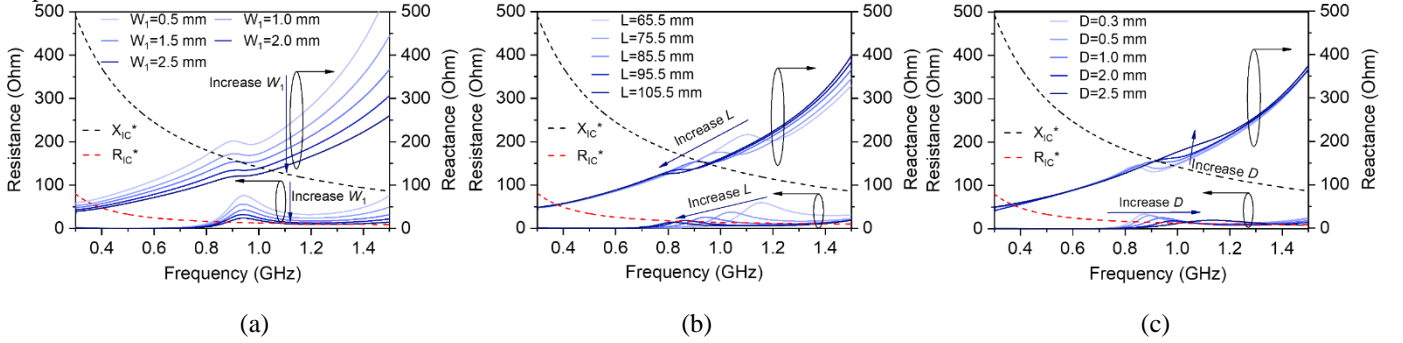


Fig. 6. The simulated resistance ( $R$ ) and reactance ( $X$ ) of the proposed antenna for different (a)  $W_1$ , (b)  $L$  and (c)  $D$ .  $X_{IC}^*$  and  $R_{IC}^*$  are the conjugate reactance and resistance of the RFID.

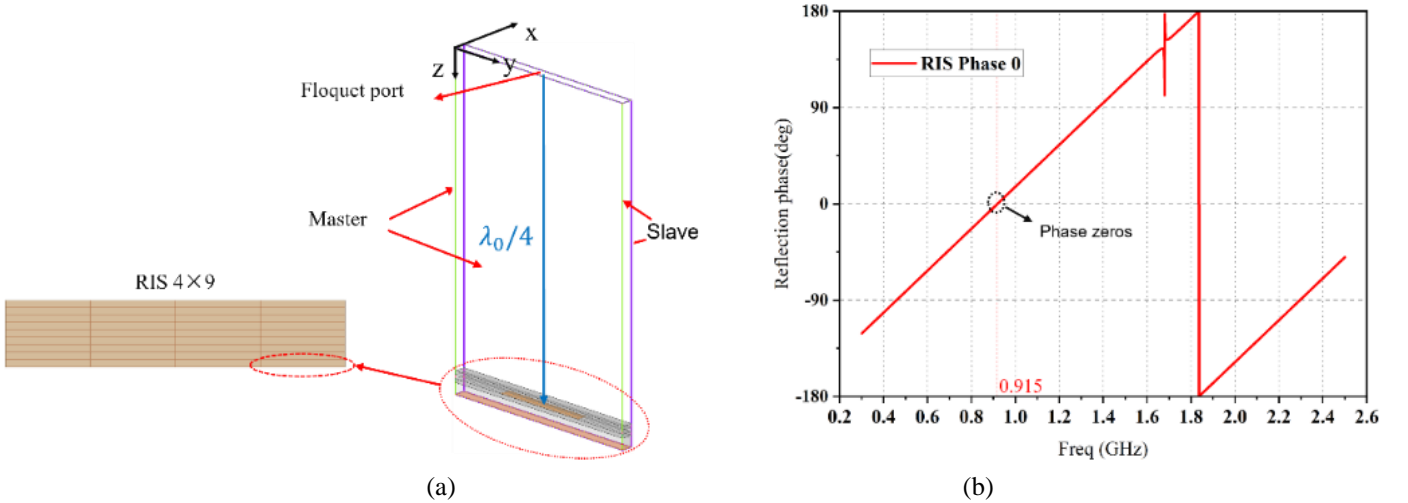
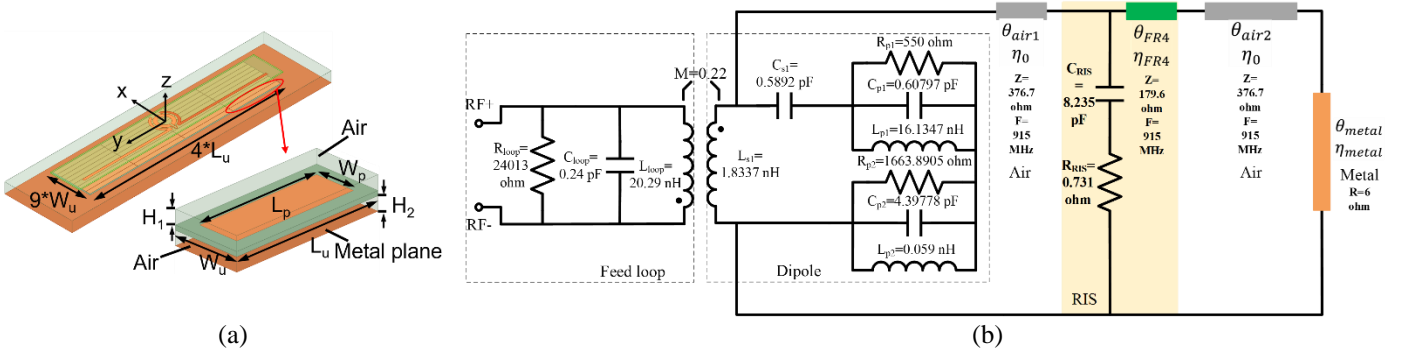


Fig. 7. (a) Topology of RIS Simulation model. (b) Reflection phase of the MS under x-/y- polarized plane wave, the red curve represents the 0-phase point after adjusting the RIS ( $L_u=57$  mm,  $W_u=3$  mm,  $L_p=26$  mm,  $W_p=2.8$ ).



> IoT-53036-2025 <

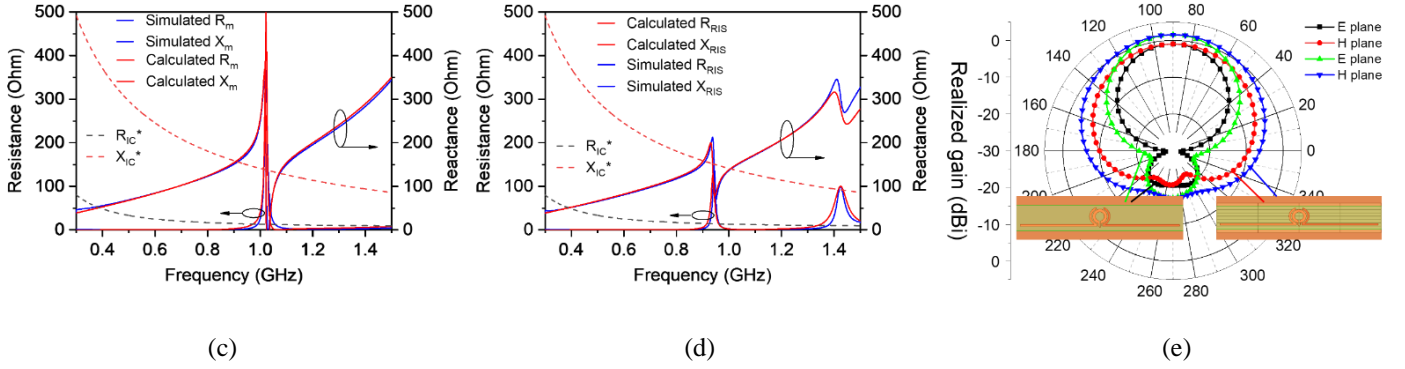


Fig. 8. (a) Illustration of the proposed antenna configuration.  $H_1=1$  mm,  $H_2=3$  mm,  $W_u=4$  mm,  $L_u=46$  mm,  $W_p=3.8$  mm,  $L_p=45.8$  mm. (b) The lumped element/transmission line hybrid equivalent circuit of the proposed FWD+RIS+Metal-Plane configuration. The comparison of the simulated resistance ( $R_m$ ) and reactance ( $X_m$ ) of the inductively fed dipole located above the metal in HFSS and ADS (c) without RIS and (d) with RIS.  $X_{IC}^*$  and  $R_{IC}^*$  are the conjugate reactance and resistance of the RFID IC. (e) The simulated realized gain of the inductively fed dipole located above the metal without RIS (marked by squares) and with RIS (marked by triangles) in  $E$  plane( $xoz$ ) and  $H$  plane( $yo$ z).

### B. RIS for Metal-mounted RFID Tag Applications

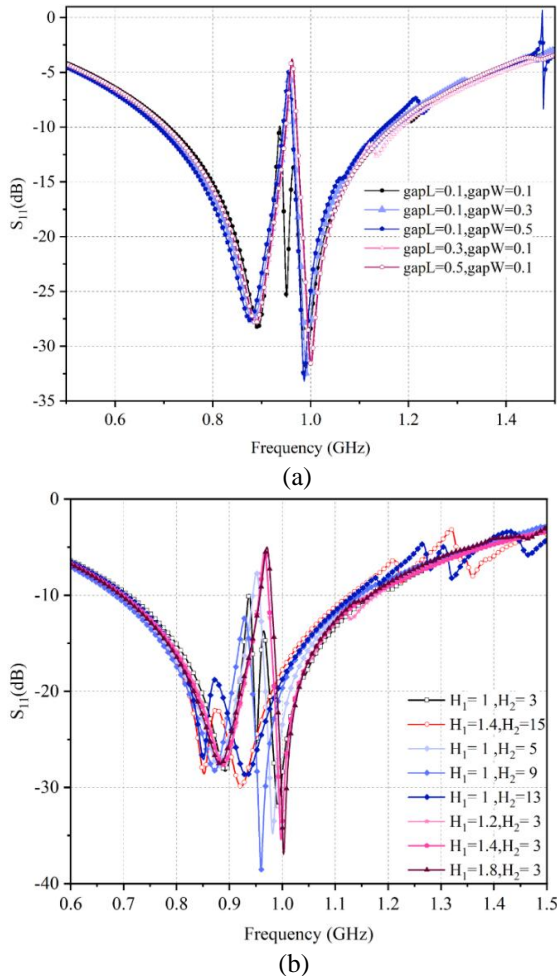


Fig. 9. (a) Simulated return loss curves  $S_{11}$  as the edge spacing gaps between the RIS rectangular metal sheet named  $gapL$  ( $2*gapL=L_u-L_p$ ) and  $gapW$  ( $2*gapW=W_u-W_p$ ) vary. (b) Simulated return loss curves  $S_{11}$  as the proposed antenna with the distance between the proposed antenna and RIS( $H_1$ ), and the distance between the metal Plane and RIS( $H_2$ ). The simulation frequency is 915 MHz. (All units are in mm)

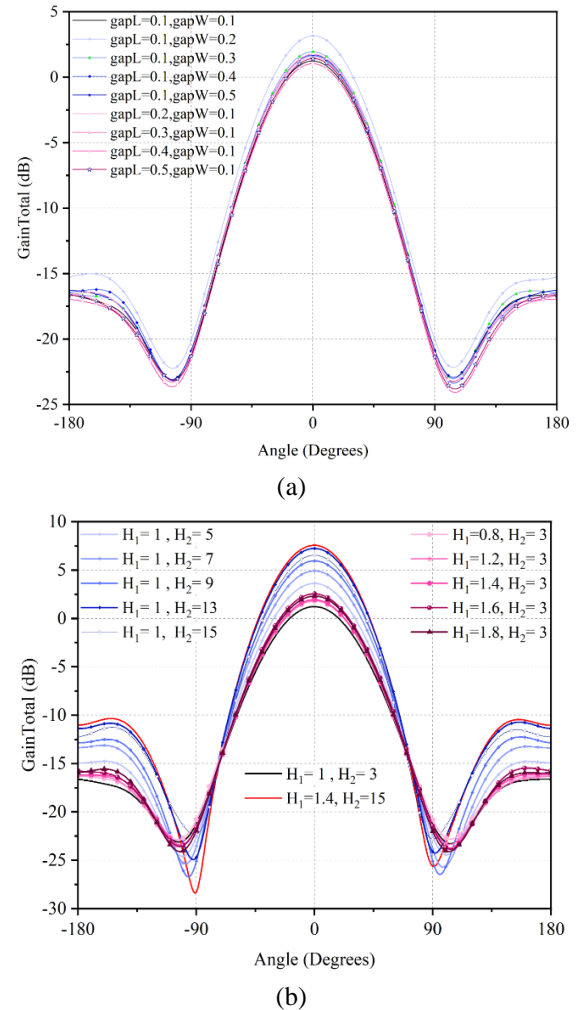


Fig. 10. (a) Simulated gain curves as the edge spacing gaps between the RIS rectangular metal sheet named  $gapL$  ( $2*gapL=L_u-L_p$ ) and  $gapW$  ( $2*gapW=W_u-W_p$ ) vary. (b) Simulated gain curves as the proposed antenna with the distance between the proposed antenna and RIS( $H_1$ ), and the distance between the metal Plane and RIS( $H_2$ ). The simulation frequency is 915 MHz. (All units are in mm)



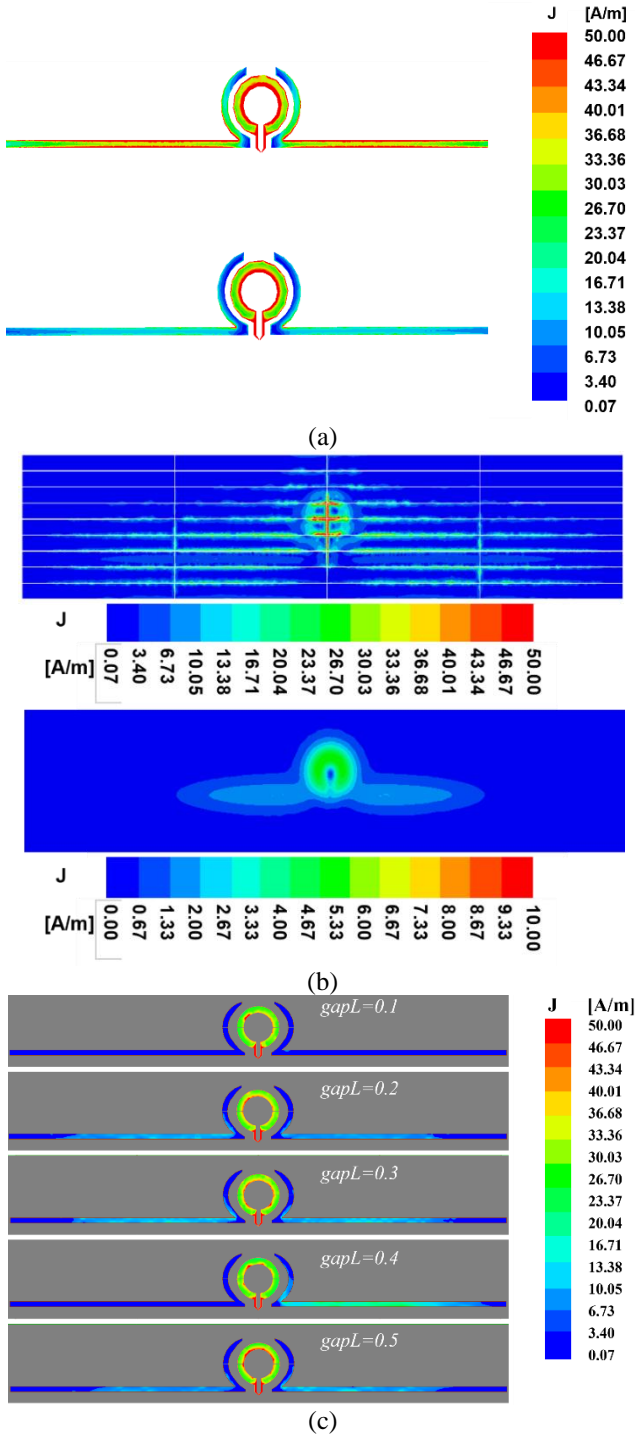


Fig. 11. (a) Current density distributions of the inductively fed dipole above the metal surface; with RIS (upper) and without RIS (lower) at 915 MHz. (b) Current density distributions: on the metal patch of the RIS (upper) and on the metal plane without RIS (lower) at 915 MHz. (c) Current density distributions with variations in the RIS  $gapL$  at 915 MHz.

Fig. 7(a) presents the structural schematic diagram of the RIS unit and the dispersion simulation setup. A metal plate simulates the back metal network in the prefabricated component traceability environment, positioned 5 mm from the antenna ( $H_1 = 1$  mm,  $H_2 = 3$  mm). The RIS's electromagnetic

wave regulation performance can be observed by examining the reflection phase at one quarter wavelength. As illustrated in Fig. 7(b), with  $L_p = 26$  mm, and  $W_p = 2.8$  mm, a zero-phase point is achieved at the frequency of interest, 915 MHz, indicating phase regulation capability. A  $4 \times 9$  RIS array is then configured below the antenna to form a new tag structure, as shown in Fig. 8(a). Similarly, a  $400 \times 150 \times 1$  mm<sup>3</sup> metal plane is placed 5 mm below the tag; the corresponding simulated impedances are given in Figs. 8(c) and (d). To clearly illustrate the RIS role, the impedance and gain (Fig. 8c) of the tag without loading (Fig. 8a) and with loading RIS (Fig. 8b) are compared. It can be observed that the resistance of the antenna without RIS increases sharply, and the reactance fluctuates violently around the full-wave resonance, which has shifted to 1 GHz. Due to mismatch and stored electric field energy between the dipole and the metal plane, the maximal simulated realized gain is about -0.98 dBi. This performance deterioration stems from impedance mismatch and non-radiative field confinement between the dipole and metal surface. In contrast, the impedance deterioration of the RIS-loaded antenna is effectively alleviated, yielding an enhanced maximum simulated peak gain of 1.55 dBi. This improvement is directly derived from the customized electromagnetic interaction enabled by the RIS structure.

To further analyze the impedance characteristics, a hybrid lumped equivalent circuit combining lumped elements and transmission lines was modeled, as illustrated in Fig. 8(b). The metal plane is represented by a transmission line with electric length,  $\theta_{metal}$ , and characteristic impedance,  $\eta_{metal}$ .  $\theta_{metal}$  is set to  $180^\circ$  to align with the reflection phase of the metal at the full-wave resonant frequency, while  $\eta_{metal}$  is maintained at a few Ohms to account for leakage currents and conductive losses. The two air layers are modeled as transmission lines sharing characteristic impedance  $\eta_0$  (free-space impedance), with electric length,  $\theta_{air1}$  and  $\theta_{air2}$  determined by  $H_1$  and  $H_2$ , respectively. The patch array is characterized as an RC network in series with a transmission line featuring impedance  $\eta_{FR4}$  and electric length  $\theta_{FR4}$ . The equivalent circuit of the RIS is connected in parallel with an inductance  $L_{s1}$ .

As shown in Figs. 8(c) and 8(d), the simulation results from ADS and HFSS exhibit strong agreement, with variations in the extracted lumped element values, revealing the underlying operational mechanism. The inductance  $L_{s1}$  decreases from 16.1 nH in free space to 2.3 nH when proximity-coupled to the metal plane, attributable to enhanced parasitic capacitance between the antenna and metal plane. This capacitance effect also explains the upward frequency shifts of the full-wave resonance to 1 GHz. Concurrently, the coupling coefficient  $M$  increases from 0.31 to 0.54, indicating intensified antenna-metal interaction. Notably, when integrated with the RIS,  $L_{s1}$  further reduces to 1.8337 nH while maintaining the original 1 GHz resonance frequency. This stability arises from the RIS-metal composite structure introducing an additional parallel resonance around 1.45 GHz, as depicted in Fig. 8(d). Below the resonant frequency, the combined RIS-metal system exhibits inductive reactance that effectively counterbalances the

> IoT-53036-2025 <

parasitic capacitance. Furthermore, the coupling coefficient  $M$  decreases to 0.22 under RIS loading, demonstrating suppressed mutual coupling with image currents.

Further investigation of the influence of RIS physical parameters on antenna performance is conducted. Fig. 9 systematically illustrates the relationships between structural dimensions and bandwidth characteristics. Variations in RIS patch spacing parameters ( $gapL$  and  $gapW$ ) reveal corresponding return loss in Fig. 9(a)-(b). Fig. 9(a) demonstrates that increasing  $gapL$  and  $gapW$  induces high impedance points within the bandwidth, significantly degrading impedance matching performance. Optimal suppression of these anomalies occurs at  $gapL = gapW = 0.1$  mm, achieving return loss below -10 dB across the entire bandwidth. However, practical considerations including low-profile requirements and manufacturing feasibility lead to the final selection of  $H_1 = 1$  mm and  $H_2 = 3$  mm for experimental validation. This configuration achieves effective trade-offs between physical compactness and wideband operation. Similarly, Fig. 10(a)-(b) illustrate the gain curve of the RIS structure integrated between the antenna and the metal plane, as well as the relationship between variations in the RIS structural parameters ( $gapL$ ,  $gapW$ ,  $H_1$  and  $H_2$ ). One can clearly observe that the distances ( $H_1$ ,  $H_2$ ) between the RIS, FWD, and the metal backside exert a significant impact on gain enhancement—with the RIS spacing parameter ( $gapL$ ,  $gapW$ ) also demonstrating a notable influence. This is partly because even minor variations in the spacing parameter can induce measurable effects. However, due to the low-profile design requirement, we did not select the structural parameters that would yield the maximum gain. By comprehensively considering the previous bandwidth and gain, the final structural parameters of the RIS were determined as  $gapL = 0.1$  mm,  $gapW = 0.1$  mm,  $H_1 = 1$  mm, and  $H_2 = 3$  mm. Notably, all dimensional adjustments maintain minimum 0.1 mm increments to accommodate PCB fabrication tolerances.

Further investigation of the RIS-metal optimization mechanism involved conducting electromagnetic field simulations. Current density ( $J$ ) and electric field intensity ( $E$ ) distributions were simulated to validate the operational principles. As shown in Fig. 11(a), the feed loop exhibits comparable current densities for both metal-proximity and RIS-loaded configurations. However, the dipole arms current density increases substantially in the RIS-integrated design, confirming enhanced full-wave resonance excitation for efficient radiation. Fig. 11(b) compares current distribution on the RIS patch array and the metal plane in the baseline (non-RIS) configuration. The RIS demonstrates edge-concentrated current flow along its patch elements, contrasting with the localized current clustering beneath the antenna in the metal-backed case, consistent with prior theoretical analysis. As shown in Figure 11(c), as  $gapL$  varies, the surface current distribution of the FWD exhibits a trend of first increasing and then decreasing. This is attributed to the inhibitory effect of the RIS structure on the parasitic capacitance induced by the metal backside. Furthermore, Fig. 12(a) demonstrates intensified outward radiation in the E-field pattern of the RIS-integrated

design, which directly correlates with the observed gain improvement achieved through optimized energy redirection. As illustrated in Figure 12(b), adjusting the gap of the RIS allows for significant regulation of the coupling feed between the feed loop and the coupling arcs. This, in turn, enhances the outward radiation gain of the FWD when it is subject to interference from metal surfaces. Although a 0.1 mm variation in  $gapL$  corresponds to an extremely small change relative to the operating wavelength, adjustments to the RIS structural parameters exert a significant influence on the coupling strength  $M$  between the feed loop and coupling arcs in the FWD. Furthermore, such adjustments effectively mitigate the impact of interference from both the metal backside and the FWD itself on the near-field coupling strength.

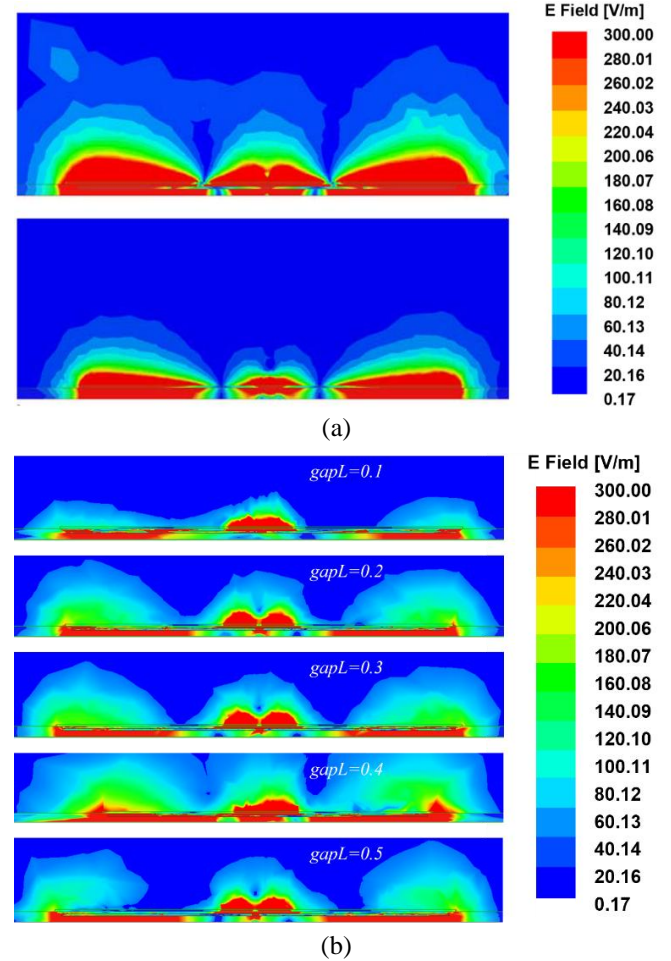


Fig. 12. (a) Electric field intensity ( $E$ ) distributions with RIS (upper) and without RIS (lower) in E plane at 915 MHz. (b) Electric field intensity ( $E$ ) distributions with the variation diagram of the  $gapL$  of RIS in E plane at 915 MHz.

In conclusion, the introduction of RIS enhances the current density on the antenna dipole arms. Additionally, it strengthens the field radiation distribution along the  $z$ -axis of the tag. This is because the RIS, positioned between the tag and the metal plane, suppresses surface currents on the metal by increasing current density across the RIS itself while reducing current density on the metal plane. This mechanism alleviates the parasitic capacitance effect induced by the metal plane.



> IoT-53036-2025 <

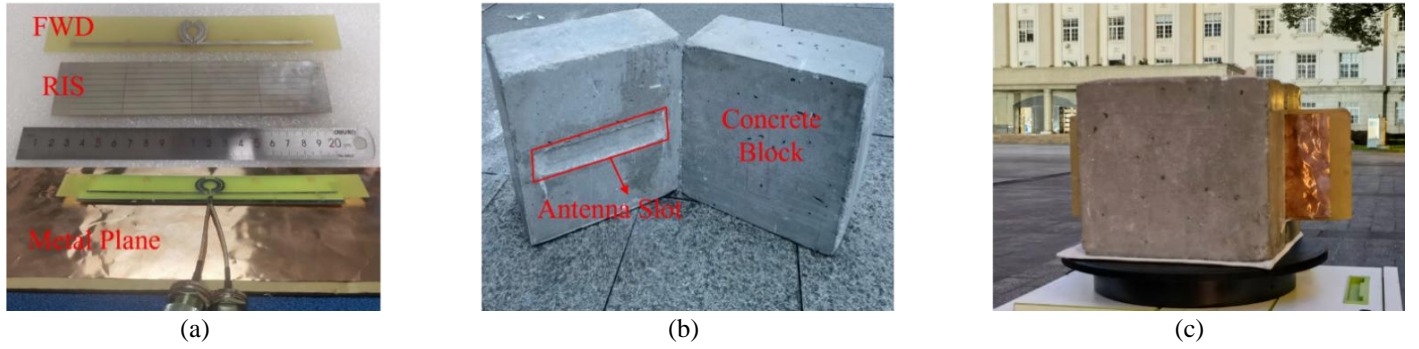


Fig. 13. Photograph of (a) the inductively fed full wave dipole, the RIS, and the Differential probe for measuring the input impedance of the proposed antenna configuration. (b) Photograph of the C30 concrete molds (the size of one is  $300 \times 300 \times 150$  mm<sup>3</sup>). (c) Photograph of the proposed antenna configuration embedded in concrete molds.

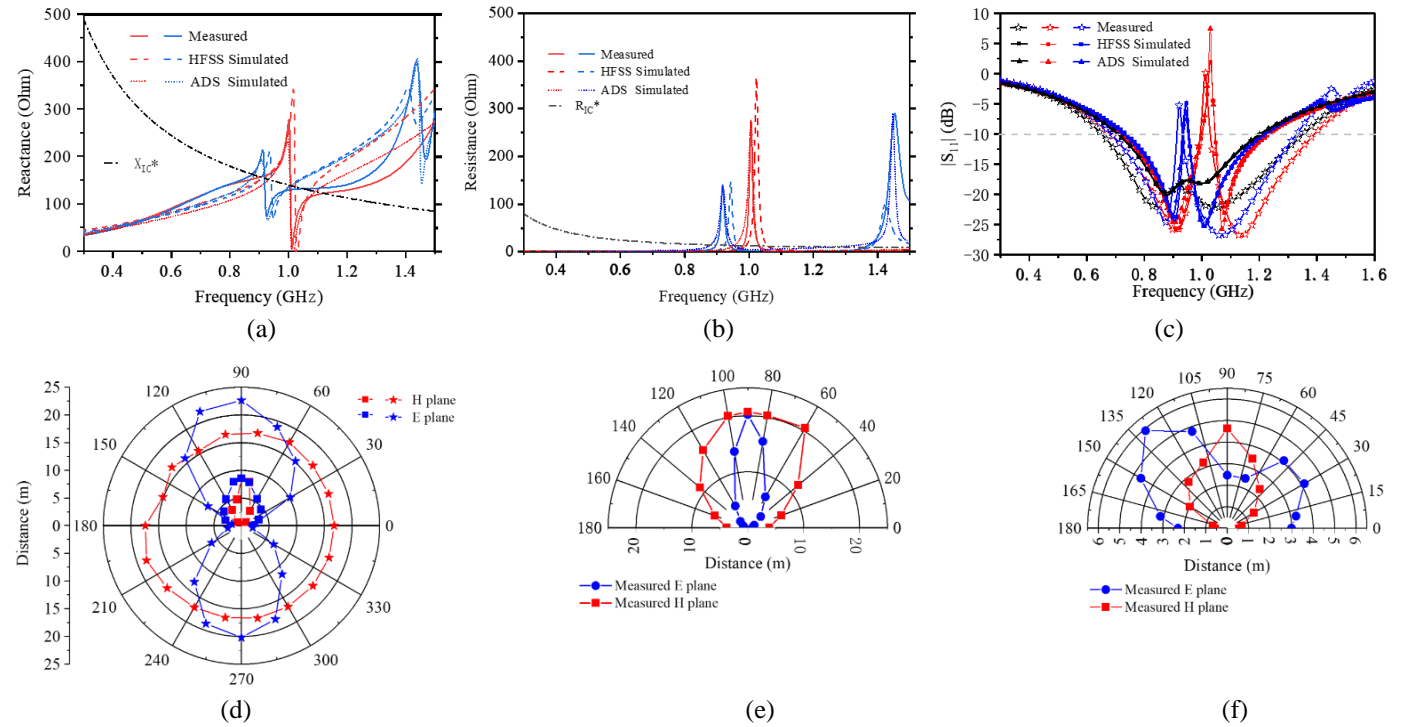


Fig. 14. (a) The measured, simulated and calculated (a) reactance and (b) resistance of the proposed antenna configuration (blue) and the inductively fed full wave dipole located above the metal without RIS (red).  $X_{IC}^*$  and  $R_{IC}^*$  are the conjugate reactance and resistance of the RFID IC. (c) The measured, simulated and calculated  $S_{11}$  of the proposed antenna configuration (blue), the inductively fed full wave dipole in located above the metal without RIS (red) and in free space (black). (d) Measured read distances in free space of the single inductively fed full wave dipole (marked by stars) and located above the metal without RIS (marked by squares) in  $E$  plane( $xoz$ ) and  $H$  plane( $yo$ z). (e) Measured read distances in free space of the antenna configuration with RIS and metal plane in  $E$  plane( $xoz$ ) and  $H$  plane( $yo$ z). (f) Measured read distances embedded in the concrete block of the antenna configuration with RIS and metal plane in  $E$  plane( $xoz$ ) and  $H$  plane( $yo$ z). The operating frequency for simulation and measurement is 915 MHz.

### III. MEASUREMENT RESULTS OF THE PROPOSED ANTENNA

Experimental validation of the proposed RFID tag configuration involved measurements with the fabricated prototype shown in Fig. 13(a). The air layer structure was realized through FR4 dielectric columns supporting the patch array between the metal ground plane and loop-fed dipole. A  $400 \times 150 \times 1$  mm<sup>3</sup> copper plate served as the metallic ground. Simulate the situation of the metal backside existing in the

concrete through the metal plane ground. Impedance characterization employed a differential probe and R&S, ZNLE6 vector network analyzer with port extension calibration. RFID read-range performance was evaluated using an Impinj, R420 reader paired with a standard 9 dBi interrogation antenna. To assess embedded performance in PCs, two  $300 \times 300 \times 150$  mm<sup>3</sup> concrete specimens were fabricated, as shown in Fig. 13(b). This concrete module was manufactured by a standard prefabrication component factory. It is of type C30 and will be put to test one month after its production. The real part of the

> IoT-53036-2025 <

relative dielectric constant is approximately 12.7, and the imaginary part is approximately 5.8 [28]. The copper-mounted antenna assembly was positioned within a machined cavity in one specimen, followed by precise specimen alignment and compression. A rotating measurement platform was employed for systematic radiation pattern characterization, as shown in Fig. 13(c). Fig. 14(a)-(c) compare measured and simulated impedance characteristics and  $S_{11}$  responses. Relative to simulation, the full-wave resonance frequency of the metal-mounted loop-fed dipole without RIS shifts slightly from 1.02 GHz (simulated) to 1.0 GHz (measured). For the RIS-integrated configuration, the primary resonance shifts from 0.943 GHz to 0.917 GHz, while the RIS-induced secondary resonance shifts from 1.43 GHz to 1.45 GHz, as shown in Figs. 14(a) and (b). These frequency deviations can be attributed to the manufacturing tolerances, with PCB fabrication etching tolerances being the primary source of error. Specifically, variations in RIS  $gapL$  (designed to be 0.1 mm) due to an etching accuracy of  $\pm 0.05$  mm result in  $gapL$  ranging from 0.05 mm to 0.15 mm. This led to a resonance frequency shift of  $\sim 20$  MHz for every 0.05 mm increase in  $gapL$ , as the larger gap weakens inter-patch coupling and disrupts the balance between inductive reactance and parasitic capacitance. Additionally, tolerances in the dipole arm length ( $L = 85.5$  mm) of  $\pm 0.1$  mm result in  $\sim 5$  MHz resonance shifts per 0.1 mm increase, contributing to minor frequency offsets. These deviations are consistent with simulated and measured data. Furthermore, the observed resonance frequency deviations primarily also stem from two interrelated sources: (1) Air layer height variations ( $H_1/H_2$ ) caused by manufacturing tolerances in FR4 dielectric column supports (with a height error of  $\pm 0.2$  mm); and (2) Parasitic effects from IC soldering. Collectively, these deviations remain within the acceptable threshold for UHF RFID ( $\leq 30$  MHz). This is validated by consistent trends between simulations (e.g., frequency increase with larger gaps) and measurements. As indicated in Fig. 14(c), the measured bandwidth ( $S_{11} \leq -10$  dB) of the loop-fed dipole reaches 700 MHz, fully encompassing the UHF RFID band. It is worth noting that, this bandwidth enhancement likely stems from reduced loop reactance, potentially influenced by the measurement cable parasitic. Even under worst-case conditions, the proposed antenna maintains  $S_{11} \leq -5.17$  dB across the UHF band, with a -10 dB bandwidth spanning 632 MHz (69%), representing the broadest reported bandwidth for metal-mounted RFID tags to date. Additionally, the reading distance  $R$  is estimated by [29]:

$$P_{tag} = P_{reader} + \tau G_{tag} + G_{reader} + 20 \log_{10} \left( \frac{\lambda}{4\pi R} \right) \quad (7)$$

where  $P_{tag}$  is the RFID IC read sensitivity in dBm,  $P_{reader}$  is the reader transmit power in dBm,  $G_{tag}$  is the tag antenna gain in dBi,  $\tau$  is the polarization loss,  $G_{reader}$  is the reader antenna gain in dBi, and  $\lambda$  is the wavelength. Figure 14(d) presents the measurement results for the reading distances of a single RFID tag's  $E$ -plane (marked with a blue star) and  $H$ -plane (marked with a red star) in free space, which are consistent with the gain curves of the corresponding  $E$ -plane and  $H$ -plane of a single

antenna. Similarly, after a metal plane is added to the back of the antenna, the reading distances in the  $E$ -plane (marked with a blue circle) and  $H$ -plane (marked with a red square) are also presented in Figure 14(d). The free-space configuration achieves a maximum  $R$  of 22.62 m at 915 MHz, which plummets to 8.61 m when metal-mounted. The integration of the RIS restores performance, as shown in Fig. 14(e), yielding a maximum reading distance of  $R = 20.19$  m, which is comparable to free-space operation and confirms effective suppression of metal interference. It should be noted that the discrepancies between simulation and measurement results primarily arise from two factors in natural-environment measurements: the influence of environmental multipath effects and alignment losses between the tag and reader antennas. When embedded in concrete, the antenna achieves a maximum  $R = 4.63$  m in the  $H$ -plane, as shown in Fig. 14(f). Notably, the  $E$ -plane  $R$  profile exhibits concave curvature near  $90^\circ$ , peaking at approximately  $90 \pm 45^\circ$  due to reduced concrete thickness between antenna terminals and the mold surface.

Table I provides a comparative analysis of the proposed RFID tag antenna against recently reported on-metal tag antennas operating within RFID frequency band. To enable precise reading distance comparisons under standardized conditions, normalization calculations were performed following the methodology in [4]. The reading distance  $R$  is derived from the Friis free-space formula:

$$R = \frac{\lambda}{4\pi} \sqrt{\frac{P_{read}}{L_f P_{tag}}} \quad (8)$$

where  $L_f$  is the measured forward-link losses, which include cable and free-space path losses. Assuming equivalence between measured and normalized forward-link losses, the normalization standard adopts an equivalent isotropic radiated power (EIRP) of 4 W and a chip sensitivity of -17.8 dBm. Converting these decibel values to standard unit yields:

$$R_{norm} = R_{meas} \sqrt{\frac{P_{readnorm}}{P_{readmeas}}} 10^{(P_{tagmeas} - P_{tagnorm})/10} \quad (9)$$

Here,  $R_{norm}$  is the normalized reading distance in meter;  $R_{meas}$  (20.19 m) is the maximum read distance obtained from the experiment;  $P_{readmeas}$  (1 W) and  $P_{tagmeas}$  (-17 dBm) are the measured reader transmit power in Watts and RFID IC read sensitivity in dBm, respectively;  $P_{readnorm}$  (4 W) and  $P_{tagnorm}$  (-17.8 dBm) are the normalized reader transmit power in Watts and RFID ICs read sensitivity in dBm, respectively [4]. Given the antenna's physical size and bandwidth, a figure of merit (FOM) defined as  $FOM = \frac{R_{norm}}{Size \times 1000} * BWR$  is proposed for comparative analysis. Here, 'size' refers to electrical size, and 'BWR' denotes the -10 dB bandwidth ratio. The calculated values are presented in Table I. When accounting for volume and bandwidth, our RIS-loaded tag outperforms nine reported metal-mounted designs. It achieves both the longest normalized read distance (44.28 m) and the widest bandwidth (632 MHz, 69.45%), with its FOM ( $24.078 \text{ m}/(\lambda_0^3 \cdot 10^3)$ ) ranking first, which reflects superior comprehensive performance in balancing read range, size, and bandwidth. Additionally, considering the prefabricated component traceability, standard

> IoT-53036-2025 <

dimensions for concrete slabs and walls are typically  $3000 \times 1000 \times 100 \text{ mm}^3$  and  $6000 \times 1200 \times 150 \text{ mm}^3$ , respectively. Compared to these substantial traceability components, the volume of our tag is manageable. Thus, our tag offers significant advantages for tracing large within complex electromagnetic environments, such as prefabricated buildings, bridges, and tunnels. This performance advantage originates from three key factors: (1) Inductive coupling between the feed loop and coupling arcs effectively addresses FWD impedance matching challenges; (2) Utilization of FWD characteristics; and (3) RIS-enhanced field distribution providing backside metal tolerance. Furthermore, the antenna maintains a 4.63 m reading distance in concrete and 20.19 m in metal-embedded concrete (with RIS), outperforming counterparts in harsh media. Ultimately, the configuration delivers superior metrics: a 20.19 m reading distance, 632 MHz bandwidth (-10 dB), and 1 W EIRP efficiency — attributes critically aligned with PC tracking requirements. While exhibiting larger dimensions than some alternatives, this trade-off accommodates the substantial volume of typical PC components without compromising functionality.

#### IV. CONCLUSION

A RIS-loaded inductively fed FWD RFID tag antenna is

proposed for PCs traceability in both metal-mounted and concrete-embedded scenarios. The feed loop's impedance transformation mechanism enables effective matching between the high impedance of the FWD and the substantial capacitive reactance of the UHF RFID IC. RIS integration significantly mitigates impedance degradation and radiation deterioration when the antenna operates near metallic surfaces. A hybrid lumped-transmission line equivalent circuit model was established alongside current density and electric field simulations to validate the RIS-mediated parasitic capacitance compensation and antenna-metal decoupling mechanisms. Experimental validation confirmed a -10 dB bandwidth of 700 MHz (76.5%) and maximum reading distance of 22.62 for the single FWD in free-space operation. Under metal-mounted conditions with a  $4 \times 9$  RIS unit cell array, a maximum reading distance of 20.19 m was achieved with a -10 dB bandwidth of 632 MHz (69%). In concrete-embedded implementations, the proposed metal-insensitive design achieves a robust 4.63 m reading distance, demonstrating reliable performance in construction material environments. Considering that the antenna volume is manageable for the traceability of large concrete prefabricated component modules, the ultra-long reading distance, anti-loss features, and anti-metal capabilities of our tag make it highly suitable for large-scale applications in scenarios such as prefabricated buildings, bridges, and tunnels.

TABLE I  
COMPARISON WITH OTHER METAL-MOUNTED UHF RFID TAGS

Ref.	Methods	Tag parameters			Measurements							
		Size ( $\lambda_0^3$ )	Peak Gain (dBi)	Bandwidth (MHz) (BWR)	Reader Gain (dBi)	EIRP (W)	Chip Sensitivity (dBm)	Metal Plate Size ( $\text{cm}^2$ )	Concrete Testing -Y(m)/N	Max. Read Distance (m)	Normalized Read Distance (m)	FOM ( $m/(\lambda_0^3 \cdot 10^3)$ )
<b>This work</b>	<b>RIS</b>	<b><math>0.558 \times 0.091 \times 0.018</math></b>	<b>1.55</b>	<b>632 (69.45%)</b>	<b>9</b>	<b>1</b>	<b>-17</b>	<b><math>15 \times 40</math></b>	<b>Y (4.63)</b>	<b>20.19</b>	<b>44.28</b>	<b>24.078315</b>
[30]	Patch	$0.358 \times 0.127 \times 0.005$	2.76	<10 (<1.1%)	6.2	4	-19.3	$20 \times 20$	N	15.8	13.29	0.64306
[31]	Patch	$0.175 \times 0.185 \times 0.005$	-6.2	<10 (<1.1%)	\	4	-20.5	$20 \times 20$	N	8.44	6.19	0.42064
[32]	Patch	$0.122 \times 0.122 \times 0.010$	-4.51	<30 (<3.3%)	8	4	-17.8	$20 \times 20$	N	9.5	9.5	2.10639
[3]	EBG	$0.218 \times 0.097 \times 0.021$	1.79	116 (12.75%)	\	4	-16	$30 \times 30$	N	12.3	15.13	4.343925
[33]	Dipole	$0.315 \times 0.094 \times 0.023$	-3.6	80 (8.8%)	\	4	-18.5	$35 \times 25$	N	14.6	13.47	1.74064
[12]	HIS	$0.085 \times 0.042 \times 0.001$	-11.2	25 (2.75%)	\	4	-15	$20 \times 20$	N	2	2.76	21.260525
[10]	AMC	$0.728 \times 0.546 \times 0.152$	6.46	<30 (<3.3%)	\	4	-24	\	N	23.74	11.63	0.00627
[34]	PIFA	$0.171 \times 0.079 \times 0.010$	-4.8	140 (15.38%)	8	4	-15	$50 \times 50$	N	4	5.52	6.284268
[4]	Non-resonating Ring	$0.061 \times 0.055 \times 0.005$	-3.53	8 (0.88%)	8	4	-17.8	$20 \times 20$	N	6.5	6.5	3.409824
[35]	Metal ground	$0.24 \times 0.21 \times 0.006$	-0.93	51 (5.57%)	\	4	-20	$20 \times 20$	N	10.4	8.07	1.486633



## REFERENCES

- [1] S. C. Li, L. D. Xu, and S. S. Zhao, "5G Internet of Things: A Survey," *Journal of Industrial Information Integration*, vol. 10, pp. 1-9, Jun 2018.
- [2] G. Castorina, L. Di Donato, A. F. Morabito *et al.*, "Analysis and Design of a Concrete Embedded Antenna for Wireless Monitoring Applications [Antenna Applications Corner]," *IEEE Antennas and Propagation Magazine*, vol. 58, no. 6, pp. 76-93, 2016.
- [3] X. P. Li, G. G. Gao, H. Zhu *et al.*, "UHF RFID Tag Antenna Based on the DLS-EBG Structure For Metallic Objects," *IET Microwaves Antennas & Propagation*, Article vol. 14, no. 7, pp. 567-572, Jun 2020.
- [4] Y. H. Niew, K. Y. Lee, E. H. Lim *et al.*, "Miniature Dipolar Patch Antenna with Nonresonating Ring for Metal-Insensitive UHF RFID Tag Design," *IEEE Transactions on Antennas and Propagation*, Article vol. 68, no. 3, pp. 2393-2398, Mar 2020.
- [5] H. Huang, X. Li, S. Liu *et al.*, "A New Method of Antenna Height Reduction Based on Half-Sized Full-Wave Dipole," *IEEE Transactions on Antennas and Propagation*, Article vol. 71, no. 8, pp. 6936-6940, Aug 2023.
- [6] G.-H. Sun, H. Wong, J. Yang *et al.*, "A Broadband Full-Wave Dipole Antenna Array," in *IEEE-APS Topical Conference on Antennas and Propagation in Wireless Communications (APWC)*, Granada, SPAIN, 2019, pp. 36-37, 2019.
- [7] L. Ukkonen, L. Sydänheimo, and M. Kivikoski, "Effects of Metallic Plate Size on the Performance of Microstrip Patch-Type Tag Antennas for Passive RFID," *IEEE Antennas and Wireless Propagation Letters*, Article vol. 4, pp. 410-413, 2005.
- [8] B. Gao and M. M. F. Yuen, "Passive UHF RFID Packaging with Electromagnetic Band Gap (EBG) Material for Metallic Objects Tracking," *IEEE Transactions on Components Packaging and Manufacturing Technology*, Article vol. 1, no. 8, pp. 1140-1146, Aug 2011.
- [9] D. Kim and J. Yeo, "Low-Profile RFID Tag Antenna Using Compact AMC Substrate for Metallic Objects," *IEEE Antennas and Wireless Propagation Letters*, Article vol. 7, pp. 718-720, 2008.
- [10] D. Kim and J. Yeo, "Dual-Band Long-Range Passive RFID Tag Antenna Using an AMC Ground Plane," *IEEE Transactions on Antennas and Propagation*, Article vol. 60, no. 6, pp. 2620-2626, Jun 2012.
- [11] D. Sievenpiper, L. Zhang, R. F. J. Broas *et al.*, "High-Impedance Electromagnetic Surfaces with A Forbidden Frequency Band," *IEEE Transactions on Microwave Theory and Techniques*, Correction vol. 48, no. 4, pp. 620-620, Apr 1999.
- [12] J. Zhang and Y. L. Long, "A Miniaturized Via-Patch Loaded Dual-Layer RFID Tag Antenna for Metallic Object Applications," *IEEE Antennas and Wireless Propagation Letters*, Article vol. 12, pp. 1184-1187, 2013.
- [13] Z. Lin, H. Niu, K. An *et al.*, "Refracting RIS-Aided Hybrid Satellite-Terrestrial Relay Networks: Joint Beamforming Design and Optimization," *IEEE Transactions on Aerospace and Electronic Systems*, Article vol. 58, no. 4, pp. 3717-3724, Aug 2022.
- [14] Z. Lin, H. Niu, Y. He *et al.*, "Self-Powered Absorptive Reconfigurable Intelligent Surfaces for Securing Satellite-Terrestrial Integrated Networks," *China Communications*, Article vol. 21, no. 9, pp. 276-291, Sep 2024.
- [15] K. An, Y. Sun, Z. Lin *et al.*, "Exploiting Multi-Layer Refracting RIS-Assisted Receiver for HAP-SWIPT Networks," *IEEE Transactions on Wireless Communications*, Article vol. 23, no. 10, pp. 12638-12657, Oct 2024.
- [16] Z. Lin, M. Guo, C. Han *et al.*, "Wireless Endogenous Security for SAGINs: Achieving Ubiquitous Access and Secure Communication in Symbiosis," vol. PP, 2025.
- [17] H. Mosallaei and K. Sarabandi, "Antenna Miniaturization and Bandwidth Enhancement Using a Reactive Impedance Substrate," *IEEE Transactions on Antennas Propagation*, vol. 52, no. 9, pp. 2403-2414, 2004.
- [18] G. Srinivas and D. Vakula, "High Gain and Wide Band Antenna Based on FSS and RIS Configuration," *Radio Engineering*, Article vol. 30, no. 1, pp. 96-103, Apr 2021.
- [19] J. Chatterjee, A. Mohan, and V. Dixit, "Broadband Circularly Polarized H-Shaped Patch Antenna Using Reactive Impedance Surface," *IEEE Antennas and Wireless Propagation Letters*, Article vol. 17, no. 4, pp. 625-628, Apr 2018.
- [20] Q. Zheng, W. Liu, Q. Zhao *et al.*, "Broadband RCS Reduction, Antenna Miniaturization, and Bandwidth Enhancement by Combining Reactive Impedance Surface and Polarization Conversion Metasurface," *IEEE Transactions on Antennas and Propagation*, Article vol. 72, no. 9, pp. 7395-7400, Sep 2024.
- [21] C. P. Yue and S. S. Wong, "Physical Modeling of Spiral Inductors on Silicon," *IEEE Transactions on Electron Devices*, vol. 47, no. 3, pp. 560-568, 2000.
- [22] A. F. McKinley, T. P. White, I. S. Maksymov *et al.*, "The Analytical Basis for The Resonances and Anti-Resonances of Loop Antennas and Meta-Material Ring Resonators," *Journal of Applied Physics*, Article vol. 112, no. 9, p. 9, Nov 2012, Art. no. 094911.
- [23] M. Hamid and R. Hamid, "Equivalent Circuit of Dipole Antenna of Arbitrary Length," *IEEE Transactions on Antennas and Propagation*, vol. 45, no. 11, pp. 1695-1696, Nov. 1997. USA
- [24] G. Marrocco, "The Art of UHF RFID Antenna Design: Impedance-Matching and Size-Reduction Techniques," *IEEE Antennas and Propagation Magazine*, Article vol. 50, no. 1, pp. 66-79, Feb 2008.
- [25] S. S. Mohan, M. H. Del, M., S. P. Boyd *et al.*, "Simple Accurate Expressions for Planar Spiral Inductances," *IEEE J. Solid-State Circuits*, vol. 34, no. 10, pp. 1419-1424, 1999.
- [26] P. Martin, R. Horn, and K. B. Atar, "A Multi-turn Twisted Inductor for On-chip Cross-talk Reduction," in *2016 IEEE International Conference on the Science of Electrical Engineering (ICSEE)*, 2016: IEEE.
- [27] X. Zhang, K. Wang, R. Gao *et al.*, "A 4-22 GHz Ultra-Wideband Low-Noise Amplifier With 0.8-1.5 dB NF and 28-31 dB Gain Enhanced by the Negative Load Impedance," *IEEE Transactions on Circuits and Systems I-Regular Papers*, Article vol. 72, no. 1, pp. 99-110, Jan 2025.
- [28] G. González-López, S. Blanch, J. Romeu *et al.*, "Debye Frequency-Extended Waveguide Permittivity Extraction for High Complex Permittivity Materials: Concrete Setting Process Characterization," *IEEE Transactions on Instrumentation Measurement*, vol. 69, no. 8, pp. 5604-5613, 2020.
- [29] A. Sharma, A. T. Hoang, F. Nekoogar *et al.*, "An Electrically Small, 16.7 m Range, ISO18000-6C UHF RFID Tag for Industrial Radiation Sources," *IEEE Journal of Radio Frequency Identification*, vol. 2, no. 2, pp. 49-54, June 2018.
- [30] B. Aslam, M. Kashif, Y. Amin *et al.*, "Low-Profile Magnetically Coupled Dual Resonance Patch Antenna for UHF RFID Applications," *Aeu-International Journal of Electronics and Communications*, Article vol. 133, p. 9, May 2021, Art. no. 153672.
- [31] F. Erman, E. Hanafi, E. H. Lim *et al.*, "U-Shaped Inductively Coupled Feed UHF RFID Tag Antenna With DMS for Metal Objects," *IEEE Antennas and Wireless Propagation Letters*, Article vol. 19, no. 6, pp. 907-911, Jun 2020.
- [32] Y. H. Lee, E. H. Lim, F. L. Bong *et al.*, "Bowtie-Shaped Folded Patch Antenna With Split Ring Resonators for UHF RFID Tag Design," *IEEE Transactions on Antennas and Propagation*, Article vol. 67, no. 6, pp. 4212-4217, Jun 2019.
- [33] A. Hamani, M. C. E. Yaoub, T. P. Vuong *et al.*, "A Novel Broadband Antenna Design for UHF RFID Tags on Metallic Surface Environments," *IEEE Antennas and Wireless Propagation Letters*, Article vol. 16, pp. 91-94, 2017.
- [34] J. Zhang and Y. L. Long, "A Dual-Layer Broadband Compact UHF RFID Tag Antenna for Platform Tolerant Application," *IEEE Transactions on Antennas and Propagation*, vol. 61, no. 9, pp. 4447-4455, Sep 2013.
- [35] W. Huang, S. Hou, J. Hu *et al.*, "A Broadband RFID Tag Antenna for Metal Surface With Characteristic Mode Analysis," *IEEE Antennas and Wireless Propagation Letters*, Article vol. 24, no. 6, pp. 1427-1431, Jun 2025.